# CryoMAE: Few-Shot Cryo-EM Particle Picking with Masked Autoencoders
## *Supplementary Material*

## A. Adjusted Self-Cross Similarity Loss Derivation

To adjust self-cross similarity loss to consider particles in unlabeled regions, we recognize that a certain proportion ($\hat{\pi}$) of the unlabeled regions contain particles. Based on this, we propose an adjustment to the self-cross similarity loss. Specifically, we modify each unlabeled region's latent feature by applying a weighting scheme based on the estimated probability ($\hat{\pi}$) that the unlabeled region contains a particle. This probability also informs the complementary weight ($1-\hat{\pi}$) for the likelihood that the region does not contain a particle.

This necessitates an additional layer of analysis. We now need to consider the self-similarity among these potential positive regions within the unlabeled data, the self-similarity between these potential positive regions and exemplars, and the cross-similarity between potential positive regions and the negative regions within the unlabeled data. This leads to the ensuing derivations of the adjusted self-similarity and cross-similarity:

$$
\begin{aligned}
\hat{S}_{self} &= \frac{1}{(m+\hat{\pi}n)^2}\Bigg[\sum_{i=1}^{m}\sum_{j=1}^{m}\left(\frac{\mathrm{E}(\hat{\mathbf{x}}_i^l)^T}{\|\mathrm{E}(\hat{\mathbf{x}}_i^l)\|}\times\frac{\mathrm{E}(\hat{\mathbf{x}}_j^l)}{\|\mathrm{E}(\hat{\mathbf{x}}_j^l)\|}\right)+\sum_{i=1}^{m}\sum_{j=1}^{n}\left(\frac{\mathrm{E}(\hat{\mathbf{x}}_i^l)^T}{\|\mathrm{E}(\hat{\mathbf{x}}_i^l)\|}\times\hat{\pi}\frac{\mathrm{E}(\hat{\mathbf{x}}_j^u)}{\|\mathrm{E}(\hat{\mathbf{x}}_j^u)\|}\right)+\\
&\qquad\sum_{i=1}^{n}\sum_{j=1}^{m}\left(\hat{\pi}\frac{\mathrm{E}(\hat{\mathbf{x}}_i^u)^T}{\|\mathrm{E}(\hat{\mathbf{x}}_i^u)\|}\times\frac{\mathrm{E}(\hat{\mathbf{x}}_j^l)}{\|\mathrm{E}(\hat{\mathbf{x}}_j^l)\|}\right)+\sum_{i=1}^{n}\sum_{j=1}^{n}\left(\hat{\pi}\frac{\mathrm{E}(\hat{\mathbf{x}}_i^u)^T}{\|\mathrm{E}(\hat{\mathbf{x}}_i^u)\|}\times\hat{\pi}\frac{\mathrm{E}(\hat{\mathbf{x}}_j^u)}{\|\mathrm{E}(\hat{\mathbf{x}}_j^u)\|}\right)\Bigg]\\
&= \frac{1}{(m+\hat{\pi}n)^2}\Bigg[\sum_{i=1}^{m}\sum_{j=1}^{m}\left(\frac{\mathrm{E}(\hat{\mathbf{x}}_i^l)^T\mathrm{E}(\hat{\mathbf{x}}_j^l)}{\|\mathrm{E}(\hat{\mathbf{x}}_i^l)\|\|\mathrm{E}(\hat{\mathbf{x}}_j^l)\|}\right)+\hat{\pi}\sum_{i=1}^{m}\sum_{j=1}^{n}\left(\frac{\mathrm{E}(\hat{\mathbf{x}}_i^l)^T\mathrm{E}(\hat{\mathbf{x}}_j^u)}{\|\mathrm{E}(\hat{\mathbf{x}}_i^l)\|\|\mathrm{E}(\hat{\mathbf{x}}_j^u)\|}\right)+\\
&\qquad\hat{\pi}\sum_{i=1}^{n}\sum_{j=1}^{m}\left(\frac{\mathrm{E}(\hat{\mathbf{x}}_i^u)^T\mathrm{E}(\hat{\mathbf{x}}_j^l)}{\|\mathrm{E}(\hat{\mathbf{x}}_i^u)\|\|\mathrm{E}(\hat{\mathbf{x}}_j^l)\|}\right)+\hat{\pi}^2\sum_{i=1}^{n}\sum_{j=1}^{n}\left(\frac{\mathrm{E}(\hat{\mathbf{x}}_i^u)^T\mathrm{E}(\hat{\mathbf{x}}_j^u)}{\|\mathrm{E}(\hat{\mathbf{x}}_i^u)\|\|\mathrm{E}(\hat{\mathbf{x}}_j^u)\|}\right)\Bigg]\\
&= \frac{1}{(m+\hat{\pi}n)^2}\Bigg[\sum_{i=1}^{m}\sum_{j=1}^{m}\left(\frac{\mathrm{E}(\hat{\mathbf{x}}_i^l)^T\mathrm{E}(\hat{\mathbf{x}}_j^l)}{\|\mathrm{E}(\hat{\mathbf{x}}_i^l)\|\|\mathrm{E}(\hat{\mathbf{x}}_j^l)\|}\right)+2\hat{\pi}\sum_{i=1}^{m}\sum_{j=1}^{n}\left(\frac{\mathrm{E}(\hat{\mathbf{x}}_i^l)^T\mathrm{E}(\hat{\mathbf{x}}_j^u)}{\|\mathrm{E}(\hat{\mathbf{x}}_i^l)\|\|\mathrm{E}(\hat{\mathbf{x}}_j^u)\|}\right)+\\
&\qquad\hat{\pi}^2\sum_{i=1}^{n}\sum_{j=1}^{n}\left(\frac{\mathrm{E}(\hat{\mathbf{x}}_i^u)^T\mathrm{E}(\hat{\mathbf{x}}_j^u)}{\|\mathrm{E}(\hat{\mathbf{x}}_i^u)\|\|\mathrm{E}(\hat{\mathbf{x}}_j^u)\|}\right)\Bigg],
\end{aligned}
$$

$$
\begin{aligned}
\hat{S}_{cross} &= \frac{1}{(m+\hat{\pi}n)(1-\hat{\pi})n}\left[\sum_{i=1}^{m}\sum_{j=1}^{n}\left(\frac{\mathrm{E}(\hat{\mathbf{x}}_i^l)^T}{\|\mathrm{E}(\hat{\mathbf{x}}_i^l)\|}\times(1-\hat{\pi})\frac{\mathrm{E}(\hat{\mathbf{x}}_j^u)}{\|\mathrm{E}(\hat{\mathbf{x}}_j^u)\|}\right)+\sum_{i=1}^{n}\sum_{j=1}^{n}\left(\hat{\pi}\frac{\mathrm{E}(\hat{\mathbf{x}}_i^u)^T}{\|\mathrm{E}(\hat{\mathbf{x}}_i^u)\|}\times(1-\hat{\pi})\frac{\mathrm{E}(\hat{\mathbf{x}}_j^u)}{\|\mathrm{E}(\hat{\mathbf{x}}_j^u)\|}\right)\right]\\
&= \frac{1}{(m+\hat{\pi}n)(1-\hat{\pi})n}\left[(1-\hat{\pi})\sum_{i=1}^{m}\sum_{j=1}^{n}\left(\frac{\mathrm{E}(\hat{\mathbf{x}}_i^l)^T\mathrm{E}(\hat{\mathbf{x}}_j^u)}{\|\mathrm{E}(\hat{\mathbf{x}}_i^l)\|\|\mathrm{E}(\hat{\mathbf{x}}_j^u)\|}\right)+\hat{\pi}(1-\hat{\pi})\sum_{i=1}^{n}\sum_{j=1}^{n}\left(\frac{\mathrm{E}(\hat{\mathbf{x}}_i^u)^T\mathrm{E}(\hat{\mathbf{x}}_j^u)}{\|\mathrm{E}(\hat{\mathbf{x}}_i^u)\|\|\mathrm{E}(\hat{\mathbf{x}}_j^u)\|}\right)\right].
\end{aligned}
$$

We define the terms $S^{ll}$, $S^{lu}$, and $S^{uu}$ to represent

$$
\sum_{i=1}^{m}\sum_{j=1}^{m}\left(\frac{\mathrm{E}(\hat{\mathbf{x}}_i^l)^T\mathrm{E}(\hat{\mathbf{x}}_j^l)}{\|\mathrm{E}(\hat{\mathbf{x}}_i^l)\|\|\mathrm{E}(\hat{\mathbf{x}}_j^l)\|}\right),
$$

$$\sum_{i=1}^{m}\sum_{j=1}^{n}\left(\frac{\mathrm{E}(\hat{\mathbf{x}}_i^l)^T\mathrm{E}(\hat{\mathbf{x}}_j^u)}{\|\mathrm{E}(\hat{\mathbf{x}}_i^l)\|\|\mathrm{E}(\hat{\mathbf{x}}_j^u)\|}\right), \text{ and}$$

$$\sum_{i=1}^{n}\sum_{j=1}^{n}\left(\frac{\mathrm{E}(\hat{\mathbf{x}}_i^u)^T\mathrm{E}(\hat{\mathbf{x}}_j^u)}{\|\mathrm{E}(\hat{\mathbf{x}}_i^u)\|\|\mathrm{E}(\hat{\mathbf{x}}_j^u)\|}\right),$$

respectively.

Formulas (1) and (2) can be simplified to the following expression:

$$\hat{S}_{self} = \frac{1}{(m+\hat{\pi}n)^2}\left[S^{ll} + 2\hat{\pi}S^{lu} + \hat{\pi}^2 S^{uu}\right],$$

$$\hat{S}_{cross} = \frac{1}{(m+\hat{\pi}n)(1-\hat{\pi})n}\left[(1-\hat{\pi})S^{lu} + \hat{\pi}(1-\hat{\pi})S^{uu}\right].$$

Based on the adjusted self-similarity and cross-similarity, the adjusted self-cross similarity loss can be derived as follows:

$$\hat{L}_{SCS}(\hat{S}_{cross}, \hat{S}_{self}) = \max\left(\tau, 1 + \alpha\cdot\hat{S}_{cross} - (1-\alpha)\cdot\hat{S}_{self}\right), \tag{1}$$

$\alpha$ balances self and cross-similarity contributions, and $\tau$ sets a minimum difference threshold between them, limiting further distinction efforts beyond it.

## B. Algorithm of Finding Optimal Threshold for Similarity Scores

This section presents our algorithm for determining the optimal threshold for truncating potential particle lists based on similarity scores.

Following the completion of the sliding process on a micrograph, these similarity scores are ranked. It is crucial to recognize the variability in the imaging states of different micrographs, where a single threshold does not work well. Therefore, we adopt a density-based method to determine the most suitable cutoff threshold for each micrograph automatically. This process involves calculating the average distance of each score to its $k$ nearest neighbors, and finding the score where the rate of change in these average distances is maximized as the cutoff threshold. The algorithm is shown below:

**Algorithm 1** Optimal Threshold Determination for Similarity Scores

**Require:** $S$ (sorted list of similarity scores), $k$ (number of nearest neighbors)
**Ensure:** $T_{idx}$ (threshold index), $T_{val}$ (threshold value)
**Procedure** DETERMINE_THRESHOLD($S$, $k$)
  Initialize $\Delta S$ as an array of zeros of length $|S|$
  **for** $i = 0$ to $|S| - 1$ **do**
    $D_i \leftarrow |S - S[i]|$
    $\Delta S[i] \leftarrow \text{mean}(\text{top-K}(D_i, k))$
  **end for**
  $\Delta_{\text{diff}} \leftarrow \text{diff}(\Delta S)$
  $T_{idx} \leftarrow \text{argmax}(|\Delta_{\text{diff}}|) + 1$
  $T_{val} \leftarrow S[T_{idx}]$
  **return** $T_{idx}, T_{val}$
**End Procedure**

## C. Details of Datasets

To ensure a fair comparison, the following EMPIAR IDs should not be used as evaluation sets, as these particles were used for pre-training by crYOLO, Topaz, or CryoTransformer:

EMPIAR IDs: 10004, 10005, 10017, 10023, 10025, 10028, 10033, 10050, 10059, 10075, 10093, 10072, 10077, 10081, 10096, 10097, 10154, 10160, 10181, 10184, 10186, 10215, 10234, 10240, 10289, 10291, 10345, 10532, 11056, 10387, 10406, 10444, 10526, 10590, 10671, 10737, 10760, 10816, 10852, 11051, 11057, 11183.

The evaluation datasets we selected are from the CryoPPP benchmark's test sets. The selection of test data considered a range of protein attributes, including type, shape, size, and overall structural attributes, which is enough to validate our methods.

The five additional unlabeled micrograph datasets sourced from the EMPIAR database include TcdA1 [2], 80S ribosome [1], AAA-ATPase [5], truncated PVY coat [3], and Chicken CALHM1 [4].

## D. Details of Baseline Methods

We compare our cryoMAE with three baseline methods crYOLO[1], Topaz [2], and CryoTransformer [3].

As for crYOLO, we use its official pre-trained model, which is an adjusted version of YOLO called PhosaurusNet. PhosaurusNet augments the original YOLO architecture by doubling the size of the feature map after layer 21, and concatenating it with the feature map from layer 13. The model is trained on a diverse and extensive collection of datasets, which encompass 18 internal datasets not available to the public, 14 datasets from EMPIAR, 10 simulated datasets, 6

[1] https://cryolo.readthedocs.io/en/stable/.
[2] https://cb.csail.mit.edu/cb/topaz/.
[3] https://github.com/jianlin-cheng/CryoTransformer/.

datasets contributed by users, and 10 particle-free datasets that exclusively contain contamination. 14 data sets from EMPIAR are 10023, 10004, 10017, 10025, 10028, 10050, 10072, 10081, 10154, 10181, 10186, 10160, 10033, and 10097. The simulated datasets are generated based on specific PDB models, namely: 1sa0, 5lnk, 5xnl, 6b7n, 6bhu, 6dmr, 6ds5, 6gdg, 6h3n, and 6mpu.

As for Topaz, we use its pre-trained resnet16_u64 model (16 layers, each layer has 64 units). It is trained on a large corpus of datasets including a wide variety of particles including EMPIAR-10025, 10028, 10096, 10215, 10234, and Toll receptor.

For the CryoTransformer model, we utilized the recommended settings from its official repository. The model was trained using micrographs of 22 proteins from the CryoPPP dataset, with each EMPIAR ID's data split into 80% for training, 10% for validation, and 10% for internal testing. The EMPIAR IDs for these 22 proteins are as follows: 11183, 11057, 11051, 10852, 10816, 10760, 10737, 10671, 10590, 10526, 10444, 10406, 10387, 10291, 10289, 10240, 10184, 10096, 10077, 10075, 10059, and 10005.

## E. CryoSPARC 3D Reconstrction Workflow

The detailed 3D reconstruction workflow using CryoSPARC is shown in Fig. 1. The workflow, from particle picking to reconstructed structure, encompasses essential steps: contrast transfer function (CTF) estimation, 2D classification, 2D class selection, *ab initio* reconstruction, and homogeneous refinement.

Initially, micrographs are imported into CryoSPARC from `.mrc` files, along with particle coordinates from `.star` files. CTF estimation is conducted on the micrographs to correct phase contrast from the microscope, which is essential for achieving high-resolution reconstructions. Following this, particles are extracted using the provided coordinates, and undergo 2D classification to segregate them into classes, discarding aberrant particles to enhance data quality. 2D class selection further ensures only high-quality particles are used. *Ab initio* reconstruction generates 3D models without prior knowledge, and homogeneous refinement polishes the model and ascertains the reconstruction resolution.

## F. More Particle Picking Results

To vividly compare particle picking results, we visualize some outcomes by crYOLO, Topaz, CryoTransformer, and cryoMAE (see Fig. 2 and Fig. 3).

Fig. 2 and Fig. 3 reveal that Topaz and CryoTransformer tend to identify a larger number of regions than the groundtruth, resulting in numerous false positives. CrYOLO frequently overlooks some particle regions, indicating a tendency to miss true positives. In contrast, cryoMAE demonstrates a balanced approach, effectively minimizing false positives while successfully identifying a greater number of true positives. Notably, crYOLO exhibits commendable performance on EMPIAR-10081, which can be attributed to the inclusion of EMPIAR-10081 particles in its pre-trained model's training set. However, its performance declines on EMPIAR-10345, a dataset not encountered during its training. This discrepancy raises concerns regarding crYOLO's ability to generalize to unseen particles, underlining a significant challenge in achieving robust generalization across diverse datasets.

## G. Performance of Fine-tuned CrYOLO and Topaz

Before cryoMAE is employed for particle picking on micrographs of a specific particle type, the model is fine-tuned using 15 particles of that type. To investigate the impact of fine-tuning on a limited number of examples on SOTA methods (crYOLO and Topaz), we conducted additional experiments. Unlike cryoMAE, which fine-tunes directly on particle exemplars, crYOLO and Topaz are designed to fine-tune on entire micrographs. Therefore, to evaluate these models under similar conditions, we fine-tuned crYOLO and Topaz on a micrograph containing the 15 particles used to fine-tune cryoMAE. The fine-tuning was performed following the official guidelines provided by the Topaz GitHub repository and the crYOLO website, using the suggested default parameters. It is important to note that this comparison is not entirely fair, as a single micrograph typically contains significantly more than 15 particles.

The results are shown in Tab. 3. As illustrated in the table, despite crYOLO and Topaz being exposed to more particle examples during fine-tuning compared to cryoMAE, their performance still lags behind that of cryoMAE. Notably, crYOLO's performance slightly declines after fine-tuning, whereas Topaz shows some improvement. This can be explained by the different approaches these models take toward the particle picking task. CrYOLO treats particle picking as an object detection task, which is inherently more complex due to the nature of the task and the sophisticated YOLO model it employs. In this setup, each micrograph is considered a single item in the dataset, making the model prone to overfitting when fine-tuned on one micrograp, thus likely accounting for its reduced performance after fine-tuning.

In contrast, Topaz, like our method, approaches the task as subregion classification. This approach is simpler, the model is less complex, and each particle within a micrograph is treated as a separate item, effectively expanding the dataset and enhancing robustness against overfitting. However, compared to our method, Topaz relies solely on class labels as the supervisory signal, which is relatively weak and does not incorporate contrastive learning. This limita-

tion can hinder the model's ability to learn robust and representative features. Our method addresses it by leveraging masking, self-supervised learning, and contrastive learning, which together facilitate the learning of more representative features, as discussed in the main paper.

## H. Sensitivity Analysis on Weight Factor for Loss

Our weight factor for loss was determined through grid search and empirical validation. Results are shown in Tab. 1.

| $(\alpha, \tau, \beta)$ | Average of | | | |
|---|---|---|---|---|
| | Prec. | Rec. | F1 sco. | Ab-ini. res. |
| $(0.5, 0.01, 3)$ | 0.536 | 0.662 | 0.584 | 11.32 |
| $(0.7, 0.02, 5)$ | **0.540** | **0.667** | **0.591** | **10.13** |
| $(0.9, 0.03, 7)$ | 0.500 | 0.624 | 0.561 | 11.85 |

Table 1. Average performance on test sets with different loss weight factors. Unit for Ab-initio reconstruction resolution is Å.

## I. Evaluate Model Performance with Different Numbers of Exemplars with *Ab initio* Reconstruction Resolution

*Ab initio* reconstruction resolution evaluates the diversity of orientations of picked particles. In our experiments, only the number of exemplars significantly impacts orientation diversity. We include *ab initio* reconstruction resolution as a metric for this experiment in Tab. 2 below.[4] Ab-initio reconstruction is quite cumbersome; for other experiments, the chosen metrics are sufficient.

| EMPIAR ID | 1 | 5 | 15 | 25 |
|---|---|---|---|---|
| 10081 | 16.51 | 12.68 | **11.32** | 11.34 |
| 10093 | 17.13 | 10.75 | 9.02 | **9.01** |
| 10345 | 19.40 | 11.81 | **10.27** | 10.53 |
| 10532 | 16.32 | 11.01 | **9.92** | 10.06 |
| Average | 17.34 | 11.56 | **10.13** | 10.24 |

Table 2. (Continuation of Table 6 in the Main Paper) *Ab-initio* reconstruction resolution (Å) with various exemplar numbers.

## J. The Selection of $\hat{\pi}$

The symbol $\hat{\pi}$ denotes a prior estimate of the proportion of particle regions within randomly selected regions. This can be estimated by the formula $\hat{\pi} \approx \frac{k \times p}{t}$, where $k$ is the number of pixels around a particle region's center that can be accepted as the particle's central pixel, $p$ is the estimated number of particles in a micrograph, and $t$ is the total region number in a micrograph.

We calculated this ratio for micrographs of multiple particles (excluding particles in our test set) and concluded that 0.018 is a generally acceptable value. However, this value may be tailored for improved outcomes with specific datasets if preliminary insights are available. In this context, we proceed under the assumption that our knowledge of our test set is limited to a few labeled examplars. Consequently, we have opted to maintain the value at 0.018.

## K. Overview of EMPIAR

EMPIAR is the sole source of publicly available raw cryo-EM data. CryoPPP is more like a collection of many protein datasets from EMPIAR than a single dataset. Even though there might be different datasets other than CryoPPP, these data all originate from the same EMPIAR source, with variations only in preprocessing and annotation methods.

## L. Code Availability

Our code is available at: `https://github.com/xulabs/aitom`.

## References


[1] Andreas M Anger, Jean-Paul Armache, Otto Berninghausen, Michael Habeck, Marion Subklewe, Daniel N Wilson, and Roland Beckmann. Structures of the human and drosophila 80s ribosome. *Nature*, 497(7447):80–85, 2013. 2

[2] Christos Gatsogiannis, Alexander E Lang, Dominic Meusch, Vanda Pfaumann, Oliver Hofnagel, Roland Benz, Klaus Aktories, and Stefan Raunser. A syringe-like injection mechanism in photorhabdus luminescens toxins. *Nature*, 495(7442):520–523, 2013. 2

[3] Luka Kavčič, Andreja Kežar, Neža Koritnik, Magda Tušek Žnidarič, Tajda Klobučar, Žiga Vičič, Franci Merzel, Ellie Holden, Justin LP Benesch, and Marjetka Podobnik. From structural polymorphism to structural metamorphosis of the coat protein of flexuous filamentous potato virus y. *Communications Chemistry*, 7(1):14, 2024. 2

[4] Johanna L Syrjanen, Kevin Michalski, Tsung-Han Chou, Timothy Grant, Shanlin Rao, Noriko Simorowski, Stephen J Tucker, Nikolaus Grigorieff, and Hiro Furukawa. Structure and assembly of calcium homeostasis modulator proteins. *Nature structural & molecular biology*, 27(2):150–159, 2020. 2

[5] Yanan Zhu, Wei Li Wang, Daqi Yu, Qi Ouyang, Ying Lu, and Youdong Mao. Structural mechanism for nucleotide-driven remodeling of the aaa-atpase unfoldase in the activated human 26s proteasome. *Nature communications*, 9(1):1360, 2018. 2


[4] The micrographs for EMPIAR-11056 were not available in the `.mrc` format, precluding us from performing a 3D reconstruction for this particle.

Table 3. Performance comparison of fine-tuned crYOLO (indicated by *), fine-tuned Topaz (indicated by *), non-fine-tuned crYOLO (without *), non-fine-tuned Topaz (without *), and our proposed cryoMAE.

| EMPIAR ID | Precision | | | | | Recall | | | | | F1 score | | | | | Resolution (Å) | | | | |
|---|---|---|---|---|---|---|---|---|---|---|---|---|---|---|---|---|---|---|---|---|
| | crYOLO* | Topaz* | crYOLO | Topaz | Ours | crYOLO* | Topaz* | crYOLO | Topaz | Ours | crYOLO* | Topaz* | crYOLO | Topaz | Ours | crYOLO* | Topaz* | crYOLO | Topaz | Ours |
| 10081 | 0.702 | 0.418 | **0.705** | 0.412 | 0.645 | 0.853 | 0.863 | 0.867 | 0.855 | **0.939** | 0.770 | 0.563 | **0.777** | 0.556 | 0.765 | 12.39 | 12.41 | 12.25 | 12.72 | **11.32** |
| 10093 | 0.379 | 0.341 | 0.380 | 0.328 | **0.383** | 0.357 | 0.267 | 0.355 | 0.209 | **0.497** | 0.368 | 0.299 | 0.367 | 0.255 | **0.433** | 11.66 | 11.59 | 11.64 | 11.62 | **9.02** |
| 10345 | 0.443 | 0.216 | 0.441 | 0.195 | **0.473** | 0.554 | **0.738** | 0.561 | 0.732 | 0.733 | 0.492 | 0.334 | 0.494 | 0.308 | **0.575** | 11.82 | 10.35 | 11.63 | 10.39 | **10.27** |
| 10532 | 0.487 | 0.410 | 0.501 | 0.387 | **0.503** | 0.227 | 0.373 | 0.231 | 0.311 | **0.497** | 0.310 | 0.391 | 0.316 | 0.345 | **0.500** | 12.90 | 10.59 | 12.86 | 10.85 | **9.92** |
| 11056 | 0.678 | 0.471 | 0.690 | 0.453 | **0.694** | 0.452 | 0.611 | 0.465 | 0.578 | **0.671** | 0.542 | 0.532 | 0.556 | 0.507 | **0.682** | - | - | - | - | - |
| Average | 0.538 | 0.371 | **0.543** | 0.355 | 0.540 | 0.489 | 0.570 | 0.496 | 0.537 | **0.667** | 0.496 | 0.424 | 0.502 | 0.394 | **0.591** | 12.19 | 11.24 | 12.10 | 11.40 | **10.13** |

* The micrographs for EMPIAR-11056 were not available in the *.mrc* format, precluding us from performing a 3D reconstruction for this particle.

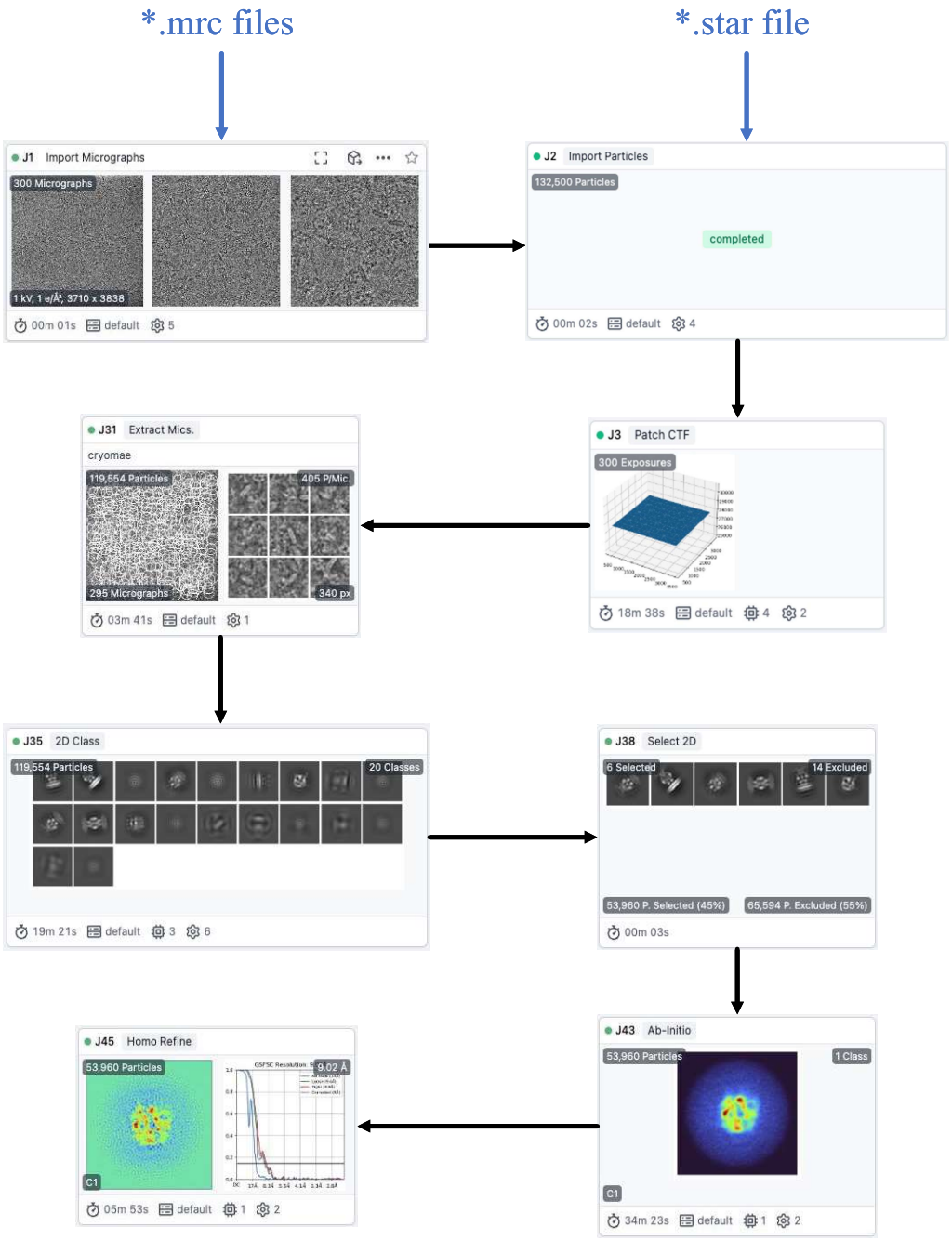


Figure 1. CryoSPARC 3D reconstrction workflow.

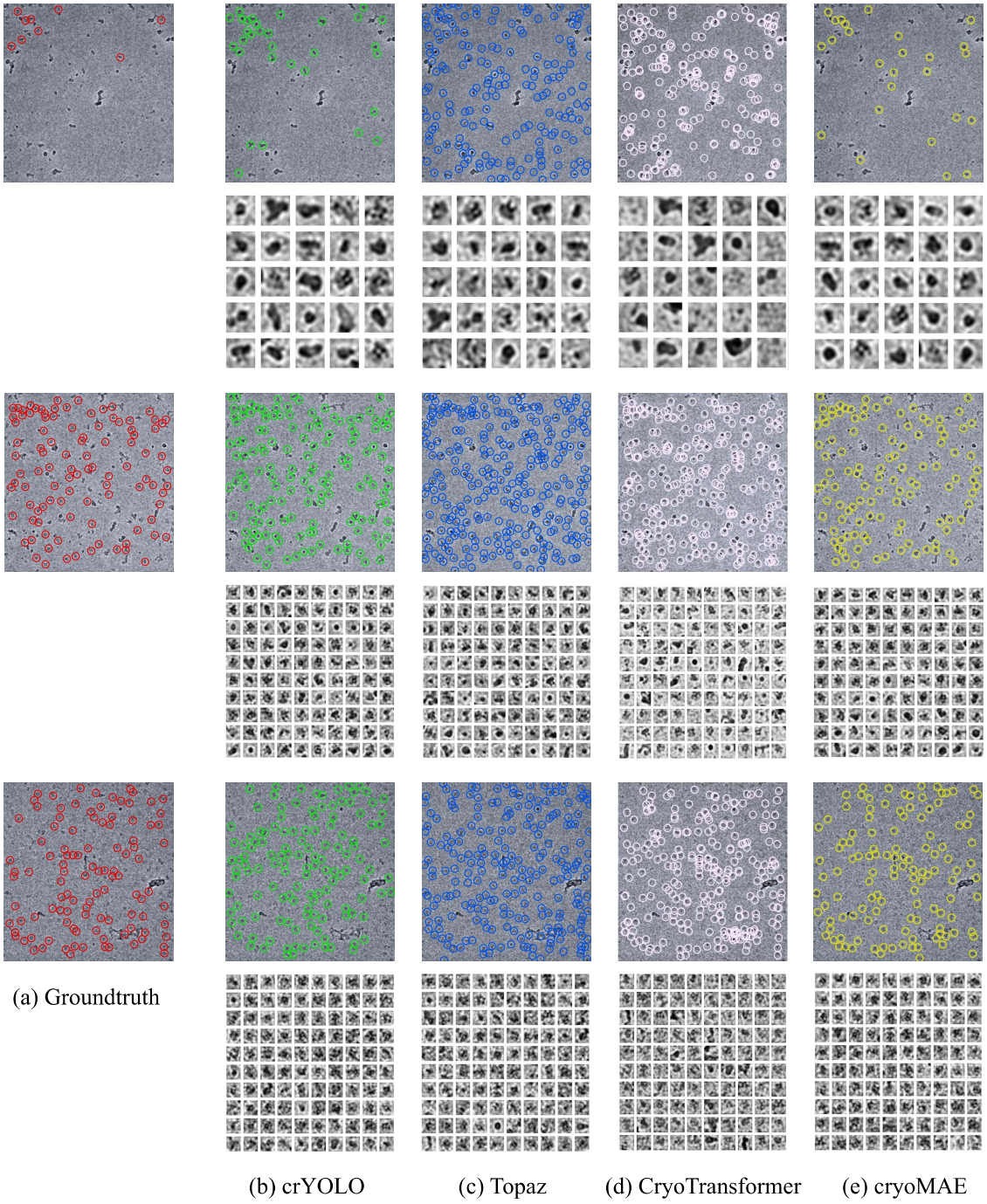


Figure 2. Particle picking results on EMPIAR-10081 by crYOLO, Topaz, CryoTransformer, and cryoMAE.

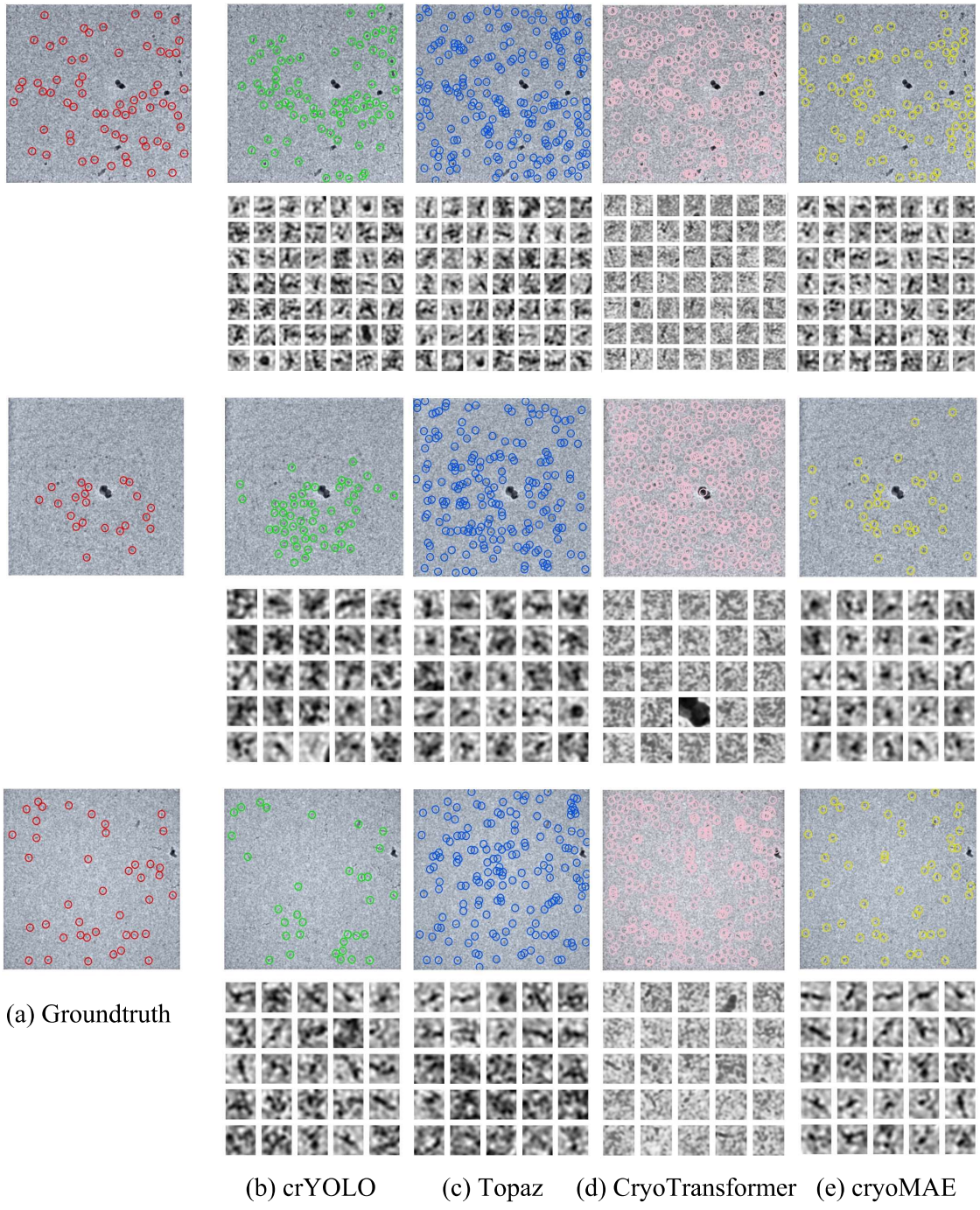


Figure 3. Particle picking results on EMPIAR-10345 by crYOLO, Topaz, CryoTransformer, and cryoMAE.